bioRxiv preprint doi: https://doi.org/10.1101/2020.12.17.423253; this version posted December 18, 2020. The copyright holder for this preprint (which was not certified by peer review) is the author/funder, who has granted bioRxiv a license to display the preprint in perpetuity. It is made available under aCC-BY-NC-ND 4.0 International license.

Shape Morphing Technique Can Accurately Predict Pelvic Bone Landmarks

Michal Kuchař[a], Petr Henyš[b], Pavel Rejtar[c], Petr Hájek[a]

[a] *Department of Anatomy, Faculty of Medicine in Hradec Králové, Charles University, Šimkova 870, 500 03 Hradec Králové, Czech Republic*
[b] *Institute of New Technologies and Applied Informatics, Faculty of Mechatronics, Informatics and Interdisciplinary Studies, Technical University of Liberec, Studentská 1402/2, 461 17 Liberec, Czech Republic*
[c] *Department of Radiology, University Hospital Hradec Králové, Sokolská 581, 500 05 Hradec Králové, Czech Republic*

Abstract

Diffeomorphic shape registration allows for the seamless geometric alignment of shapes. In this study, we demonstrated the use of a registration algorithm to automatically seed anthropological landmarks on the CT images of the pelvis. We found a high correlation between manually and automatically seeded landmarks. The registration algorithm makes it possible to achieve a high degree of automation with the potential to reduce operator errors in the seeding of anthropological landmarks. The results of this study represent a promising step forward in effectively defining the anthropological measures of the human skeleton.

Keywords: CT data, Anthropometry, Geometry Segmentation, DSP2 method, non–linear registration

*Corresponding author
Email address: petr.henys@tul.cz (Petr Henyš)

bioRxiv preprint doi: https://doi.org/10.1101/2020.12.17.423253; this version posted December 18, 2020. The copyright holder for this preprint (which was not certified by peer review) is the author/funder, who has granted bioRxiv a license to display the preprint in perpetuity. It is made available under aCC-BY-NC-ND 4.0 International license.

Highlights

- The clinical CT scan is a feasible alternative to skeletal collections and body donor programs.
- Pelvic morphology is complex, sexually dimorphic and is proven to being a good demonstration model for the performance analysis of registration algorithm for automatic landmark seeding.
- The landmark seeding using registration algorithm can save time and effort in anthropological analysis.

Introduction

In order to estimate the sex, body constitution or various anomalies of the individual from his/her skeleton, anthropologists typically rely on the nonmetric or metric analyses of the dry bone [1, 2]. More recently, the stereophotogrammetric method and medical imaging have been adopted [3]. In order to obtain reliable data, it is essential to work with a reasonably large set of specimens. The gold standard is the osteological database with personal data [4, 5, 6, 7]. Nowadays it is also possible to gain access to hospital databases and thus collect an equal or even larger set of data [8, 9] which is free from any postmortal changes. Virtual anthropometry is the method of choice in forensic cases [10], for the identification of victims of disasters [11] or in museum specimens that are susceptible to damage [12].

In recent years, we have been seeing rapid progress in the use of imaging techniques in forensic anthropology. Many studies have proven their compatibility with previous research on dry bone [13, 14] and found that CT scans are a promising source of reference data in contemporary forensic investigations [15, 16, 17]. It has been demonstrated that the accuracy of defining anthropological landmarks both manually and by use of CT scans have led to similar results between them [15, 18, 19, 20, 5]. Therefore the many methods that determine the sex of an individual, as well as the physical or biomechanical properties of a population that are already established and proven for skeletal material, could also be adopted for clinical CT data.

Regardless of the bony specimen‘s origin, its processing requires time and skill. We tried to reduce the time involved by adopting the technique of shape morphing for the mass analysis of anthropometric data. We adopted a non-linear registration algorithm which automatically computes the landmark

bioRxiv preprint doi: https://doi.org/10.1101/2020.12.17.423253; this version posted December 18, 2020. The copyright holder for this preprint (which was not certified by peer review) is the author/funder, who has granted bioRxiv a license to display the preprint in perpetuity. It is made available under aCC-BY-NC-ND 4.0 International license.

positions from the ones that are pre–defined. The registration algorithm based on diffeomorphic mapping has been successfully used in brain analyses [21] but is rarely used in bone analysis [22, 23].

The study aimed to demonstrate the potential for shape registration in the automatisation of landmark seeding thus making data–gathering and evaluation easier in further studies, regardless of the researcher‘s experience. We created a set of virtual human pelvic bones and defined anatomical landmarks, which were automatically seeded by a proposed registration algorithm.

Materials and Methods

Dataset

Pelvic bone is well suited for our study because of its multifaceted morphology. Moreover, being the most sexually dimorphic skeletal element in the human body, it could further serve as a way of sex identification by using our proposed method. The basis for virtual modelling was the retrospective and anonymised DICOM files that were randomly taken from routine examinations in the Faculty hospital in Hradec Králové under ethical approval, 202010P08. The CT resolution of the data set was 1×1×1 mm (Siemens Definition AS+, Siemens Definition 128, 120-130 kV using CareDose, reconstruction kernel 80-90, bone algorithm). The inclusion criteria were: abdominal CT scans, bones without any trauma and an age range of 20 years or older. The sample population was equally balanced in terms of sex (100 males, 100 females), with the average age being 64 ± 13.5 years.

The Segmentation of Bone Geometry

The pelvic bone geometries were obtained from CT scans with a semi–automatic segmentation algorithm (GraphCut, MITK-GEM, [24, 25]). On the downside, the algorithm may sometimes fail in finding the exact borders between the bones (sacral bone & pelvic bones, pelvic bones & the femur) that are fused via osteophytes. Therefore, in some cases, we had to manually correct the errors in the segmentation.

Bone Registration

The purpose of image registration is to geometrically align the so called *moving image* I to the so called *fixed image* J by a suitable class of maps (see Figure 1). These maps transform each voxel $\mathbf{x}$ in the moving image $I(\mathbf{x})$ to

bioRxiv preprint doi: https://doi.org/10.1101/2020.12.17.423253; this version posted December 18, 2020. The copyright holder for this preprint (which was not certified by peer review) is the author/funder, who has granted bioRxiv a license to display the preprint in perpetuity. It is made available under aCC-BY-NC-ND 4.0 International license.

the corresponding voxel $\mathbf{y}$ in the fixed image $J(\mathbf{y})$ by minimising a cost function that expresses the differences between $I(\mathbf{x})$ and $J(\mathbf{y})$ [26]. These transformations were computed by a well–known diffeomorphism method SYN in library ANTs with a modified intensity based criterion called the "demons-like metric" [27, 28]. The algorithm worked in the four–step resolution [100, 100, 50, 30] (the numbers in parentheses represent maximum optimisation iterations [1]. In this study, we used those transformations to map anatomical landmarks from template shape onto a sample shape and vice versa[2], see the convention in [26]. A suitable template bone must be created in such a way,

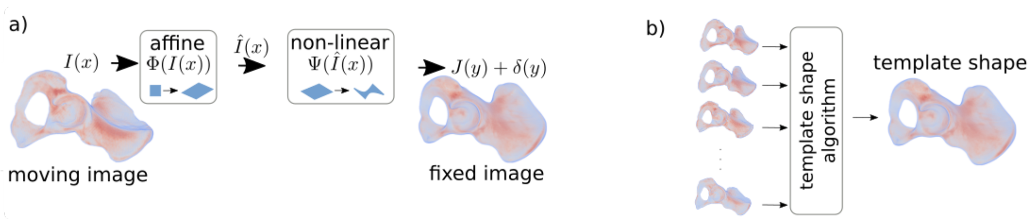

Figure 1: a) An illustration of the steps of the registration algorithm: the affine transform globally translates, rotates, scales and shears the moving image; the non–linear transform deforms (voxel–wise) the moving image in order to align the moving image with the fixed image. b) The fixed image is a template shape that is estimated from the dataset.

that it minimises the anatomical discrepancies between the template bone and any sample it is morphed into. The template bone shape was iteratively estimated according to [27]. Once the template bone was obtained, all the samples in the dataset were morphed into the template bone shape. Each morphed bone sample was visually inspected for the presence of any errors.

Anthropological Measures

The template bone was set by a group of anthropometric reference landmarks $B_1, B_2, ..., B_{19}$ with the associated distances $M_1, M_2, ..., M_{10}$ (see Table 1 and Figure 2), by utilizing ParaView software [29]. We adopted the landmarks defined by Murail and Bruzek [30], both for their acceptance in the published literature [31] as well as for following the sex–specificity test. One

[1] see the details in ANTs manual at URL: `https://antspyx.readthedocs.io`)
[2] The points are transformed in the reverse direction unlike the images

bioRxiv preprint doi: https://doi.org/10.1101/2020.12.17.423253; this version posted December 18, 2020. The copyright holder for this preprint (which was not certified by peer review) is the author/funder, who has granted bioRxiv a license to display the preprint in perpetuity. It is made available under aCC-BY-NC-ND 4.0 International license.

additional landmark B_{20} was added to test the accuracy of the algorithm on the concave surfaces (on the bottom of the acetabular fossa).

Table 1: Definitions of the reference landmarks B.

B_1	Symphysion; the most superior and medial point on the pubic symphysis
B_2	Anterior border of the acetabular rim at the level of the lunate surface
B_3	The most lateral point on the acetabular rim
B_4	A point on the medial margin of the pubic bone; at the level of B_4
B_5	The most inferior point of the os coxae
B_6	The most superior point of the os coxae
B_7	The posterior inferior iliac spine
B_8	A point on the anterior margin of the great sciatic notch.
B_9	The most anterior and inferior point on the ischial tuberosity
B_{10}	The furthest point on the acetabular margin from B_9
B_{11}	Anterior superior iliac spine
B_{12}	Posterior superior iliac spine
B_{13}	Anterior inferior iliac spine
B_{14}	The deepest point in the greater sciatic notch
B_{15}	The contact point of the arcuate line and the auricular surface
B_{16}	The midpoint of the anterior portion of the greater sciatic notch
B_{17}	A point on the lateral border of the acetabulum; at the level of B_{16}
B_{18}	The most inferior point on the acetabular rim in the longitudinal axis of the ischium
B_{19}	The most superior point on the acetabular rim on the longitudinal axis of the ischium

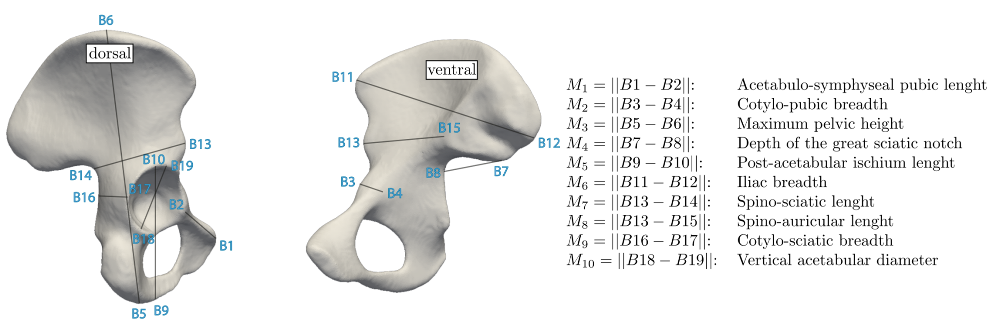

Figure 2: The estimated shape of the template bone with the reference landmarks B and distances M.

A Comparison of Manually and Automatically Seeded Landmarks

In order to evaluate the accuracy of automatic the seeding algorithm, an operator manually seeded defined landmarks on 50 bones randomly selected from dataset.

bioRxiv preprint doi: https://doi.org/10.1101/2020.12.17.423253; this version posted December 18, 2020. The copyright holder for this preprint (which was not certified by peer review) is the author/funder, who has granted bioRxiv a license to display the preprint in perpetuity. It is made available under aCC-BY-NC-ND 4.0 International license.

Intra–observer Error

We checked the consistency of manual seeding by analysing the intra–observer error in distances M. Fifty pelves were remeasured twice (test1 and test2) by a moderately experienced operator with a two week time window. The intra–observer technical error of measurement (TEM) and the percentages expressed relative rTEM were calculated. The resulting TEM index is a variable in anthropology that is used to express the margin of error and the quality of measurement. The mutual dependency of all tests is further expressed as the reliability coefficient R, that describes variance, which is free of measurement errors [32, 33, 34]:

$$\mathrm{TEM} = \sqrt{\frac{\sum_{j=1}^{n} d_j^2}{2n}}$$

$$\mathrm{rTEM} = \frac{\mathrm{TEM}}{\bar{m}} 100$$

$$\mathrm{R} = \frac{\mathrm{TEM}^2}{\sigma}$$

where n is the number of pelvis samples, $\bar{m}$ is the average distance value M, over the n samples, σ is the standard deviation over the n samples and d_j is the difference of M on the jth sample that is computed from the two measurements.

The Distance Between Automatically and Manually Seeded Landmarks, B

To analyse the differences between both automatically and manually seeded landmarks, we computed the Euclidean distance

$$\Delta_i = ||\mathbf{x}_i - \hat{\mathbf{x}}_i||$$

where $\mathbf{x}_i$ and $\hat{\mathbf{x}}_i$ are the coordinates of the ith landmark B, that were obtained manually and automatically, respectively (see Figure 3). We analysed the distances on the samples from subsection Intra–observer Error. The statistical difference between landmarks B, measured at both repetitions was measured by the Mann Whitney test with a probability level of 95%.

The differences Between Automatically and Manually Computed Distances, M

Relative differences between automatically and manually computed distances M, were analysed from samples of subsection Intra–observer Error, see

bioRxiv preprint doi: https://doi.org/10.1101/2020.12.17.423253; this version posted December 18, 2020. The copyright holder for this preprint (which was not certified by peer review) is the author/funder, who has granted bioRxiv a license to display the preprint in perpetuity. It is made available under aCC-BY-NC-ND 4.0 International license.

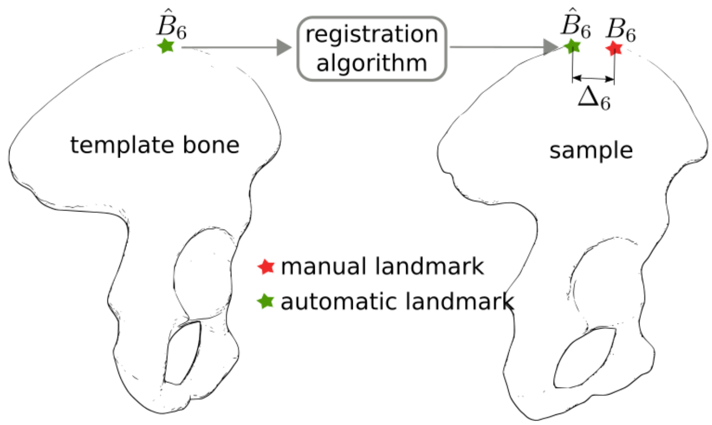

Figure 3: An example of measurement of distance between manually and automatically seeded landmark B_6.

Figure 4. The ith relative distance difference δ_r^i was computed as $100(M_i - \hat{M}_i)/\hat{M}_i$. The statistical difference between distances M, measured at both repetitions was measured by the Mann Whitney test with a probability level of 95%.

The Analysis of Clouds: the Back–Mapped Landmarks

The manually defined landmarks on the samples from subsection Intra–observer Error were mapped onto the bone template. The mapped landmarks form clouds around the reference landmarks. These landmark clouds have a certain shape, size and centroid (mean coordinates), which are used to analyze the accuracy of registration algorithms, see Figure 5. The centroids and confidence ellipsoids (eigenvalues of the covariance matrix) were estimated for the landmark clouds by the Quadratic Discriminant Classification Method (QDCM) [35]. By using the QDCM, we were able to estimate the probability that a given reference landmark belongs to the corresponding landmark cloud. The QDCM was trained by samples from subsection Intra–observer Error. The stratified KFold strategy with 3 folds and a train/test splitting at 70%/30%, was chosen in order to obtain the best accuracy [35]. The mean resultant train/test accuracy metrics were 92%±6.1%/90%±8.3%. Besides, we computed the distance Δ, between the centroids and the reference landmarks.

bioRxiv preprint doi: https://doi.org/10.1101/2020.12.17.423253; this version posted December 18, 2020. The copyright holder for this preprint (which was not certified by peer review) is the author/funder, who has granted bioRxiv a license to display the preprint in perpetuity. It is made available under aCC-BY-NC-ND 4.0 International license.

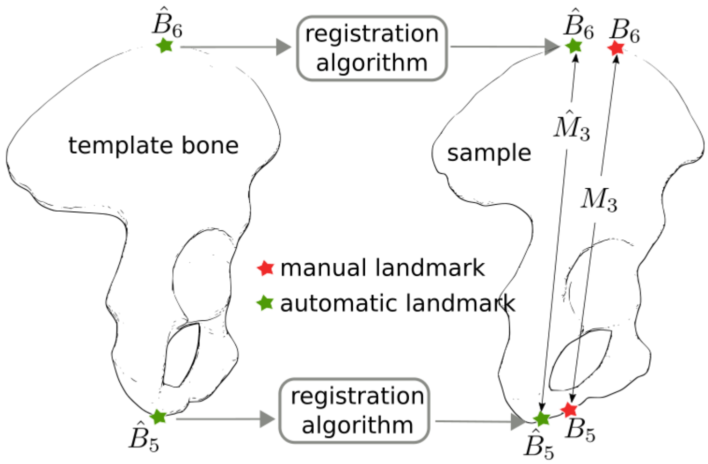

Figure 4: An example of the distance M_3 computed from the manually seeded landmarks B_5 and B_6 and the distance $\hat{M}_3$ computed from automatically seeded landmarks $\hat{B}_5$ and $\hat{B}_6$.

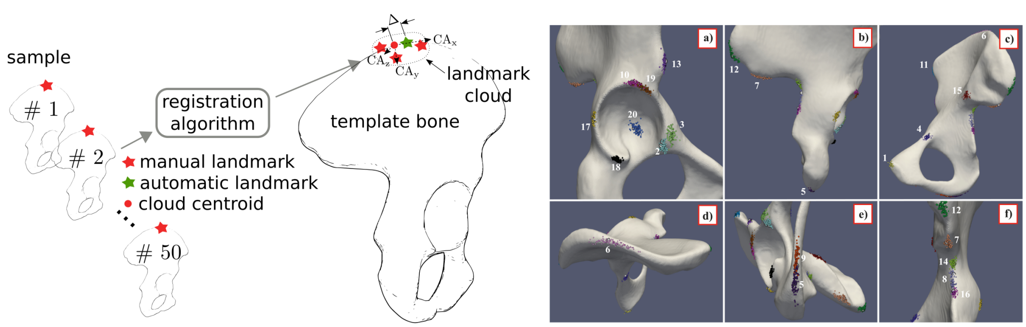

Figure 5: Use of registration algorithm for the mapping of manually seeded landmarks onto the bone template. The set [CA_x CA_y CA_z] represents eigenvalues of a 95 % confidence ellipsoid. Individually coloured clouds are shown on various aspects of the pelvic bone [a), b), c), d), e), f)]. The numbers correspond to the landmark numbers in Figure 2.

bioRxiv preprint doi: https://doi.org/10.1101/2020.12.17.423253; this version posted December 18, 2020. The copyright holder for this preprint (which was not certified by peer review) is the author/funder, who has granted bioRxiv a license to display the preprint in perpetuity. It is made available under aCC-BY-NC-ND 4.0 International license.

Sex Identification Using the DSP2 Method

We demonstrated the practical use and accuracy of the registration algorithm for sex identification. The input for the sex identification algorithm DSP2, were the distances from the subsection Intra–observer Error. DSP2 is based on a spreadsheet program (freely available at URL: `http://projets.pacea.u-bordeaux.fr/logiciel/DSP2/dsp2.html`) that gives the individual probability of being a male or female according to the linear discriminant analysis and posterior probabilities (see original publications [36, 30]). All ten distances M, served as an input to the application. The input was data consisted of 200 samples where the sex was known *a priori*.

bioRxiv preprint doi: https://doi.org/10.1101/2020.12.17.423253; this version posted December 18, 2020. The copyright holder for this preprint (which was not certified by peer review) is the author/funder, who has granted bioRxiv a license to display the preprint in perpetuity. It is made available under aCC-BY-NC-ND 4.0 International license.

Results

Observer Agreement

TEM values were in range of 0.60 for M_9 and 1.55 for M_4, see Table 2. The values of rTEM were mostly less than 2%, except for M_2 and M_4, which were 2.27 and 3.51 respectively and according to [37] are considered as being imprecise. The coefficient of reliability R, was between 0.94 and 0.99 and is defined as being high for all measurements. The TEM and rTEM were found as being relatively low [32].

Table 2: The technical and relative technical errors of manual measurements. The minimum and maximum values are in bold.

	M_1	M_2	M_3	M_4	M_5	M_6	M_7	M_8	M_9	M_{10}
TEM $[mm]$	0.79	0.98	1.16	**1.55**	0.82	1.05	1.12	1.35	**0.60**	1.02
rTEM [%]	1.07	2.27	0.53	**3.51**	0.72	**0.64**	1.44	1.70	1.59	1.77
R	0.98	0.98	**0.99**	**0.94**	0.99	0.98	0.97	0.95	0.98	0.95

The Distance Between the Automatically and Manually Seeded Landmarks, B

The largest average distance of 15.91 mm was found for landmark B_6 while the smallest distance of 2.04 mm was found for landmark B_{18} in the test set 2, see Figure 6. There were no statistically significant differences between the repetitions of test1 and test2. The lowest value of p was 0.05 for landmark B_{14}, while the highest value of 0.49 was found for landmark B_{19}.

The Differences Between the Automatically and Manually Computed Distances, M

The largest average relative difference of -4.20% was found for distance M_4 in the test set 2, see Figure 7. The average lowest relative difference of 0.01% was found for distance M_{10} in the test set 1, see Figure 7. There were no statistically significant differences between the repetitions of test1 and test2. The lowest value of p was 0.06 for the distance M_9, while the highest value of 0.49 was found for distance M_2.

The Analysis of Clouds: Back–Projected Landmarks

The longest distance of 10 mm, was found between centroid B_6 and reference landmark B_6, while the shortest distance of 0.66 mm, was found between

bioRxiv preprint doi: https://doi.org/10.1101/2020.12.17.423253; this version posted December 18, 2020. The copyright holder for this preprint (which was not certified by peer review) is the author/funder, who has granted bioRxiv a license to display the preprint in perpetuity. It is made available under aCC-BY-NC-ND 4.0 International license.

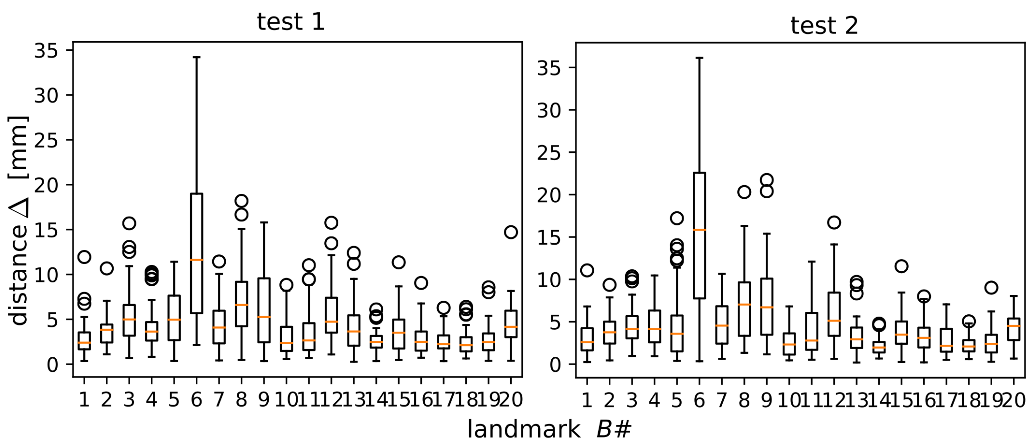

Figure 6: A boxplot showing the distance between the automatically and manually seeded landmarks for both repetitions.

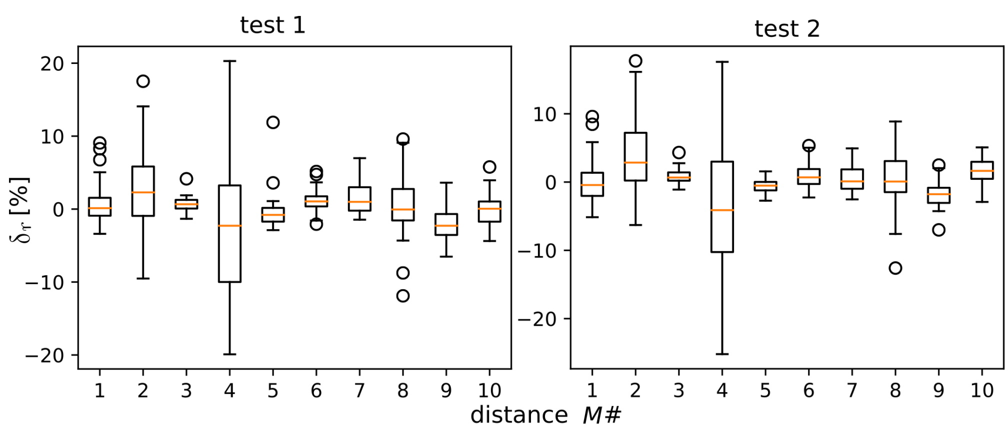

Figure 7: A boxplot showing the relative difference between automatically and manually seeded landmarks for both repetitions.

centroid B_{19} and reference point B_{19}. The distances between the centroids and the reference landmarks are in Table 3. The probability that the reference landmark falls into a given landmark cloud was high (more than 99 %) for almost all landmarks. An exception was reference landmark B_9, which fell into the landmark clouds of B_5/B_9 with a probability of 58.5%/41.5%, see Table 3. In addition, the highest length of confidence for axis x, was

bioRxiv preprint doi: https://doi.org/10.1101/2020.12.17.423253; this version posted December 18, 2020. The copyright holder for this preprint (which was not certified by peer review) is the author/funder, who has granted bioRxiv a license to display the preprint in perpetuity. It is made available under aCC-BY-NC-ND 4.0 International license.

Table 3: A comparison of the reference landmarks and centroids that are formed by a cloud of projected landmarks that were manually defined on a template bone;$\Delta[mm]$) is the distance between the reference landmarks and centroids; [CA_x CA_y CA_z] with the principal of a 95% confidence axes of an individual cloud. The minimum and maximum values are in bold.

$B\#$	Δ	CA_x	CA_y	CA_z	$B\#$	Δ	CA_x	CA_y	CA_z
B_1	0.78	1.84	2.97	5.20	B_{11}	1.20	1.40	2.58	7.11
B_2	1.98	2.89	5.11	11.81	B_{12}	2.12	**3.62**	8.83	**34.97**
B_3	4.26	0.90	3.82	7.22	B_{13}	1.63	2.68	6.24	16.38
B_4	2.01	0.80	3.52	5.79	B_{14}	0.79	2.70	3.99	16.36
B_5	0.94	1.16	2.52	11.68	B_{15}	1.19	0.69	4.62	7.58
B_6	**10.00**	1.46	3.56	24.58	B_{16}	2.03	**0.67**	2.26	4.05
B_7	2.80	1.03	2.81	9.33	B_{17}	1.27	0.79	2.02	4.82
B_8	6.92	1.14	2.64	10.34	B_{18}	1.41	0.90	**1.67**	**3.97**
B_9	5.09	1.36	**13.59**	16.32	B_{19}	**0.66**	1.05	2.06	6.84
B_{10}	1.15	1.88	2.63	10.48	B_{20}	2.50	1.03	3.79	6.02

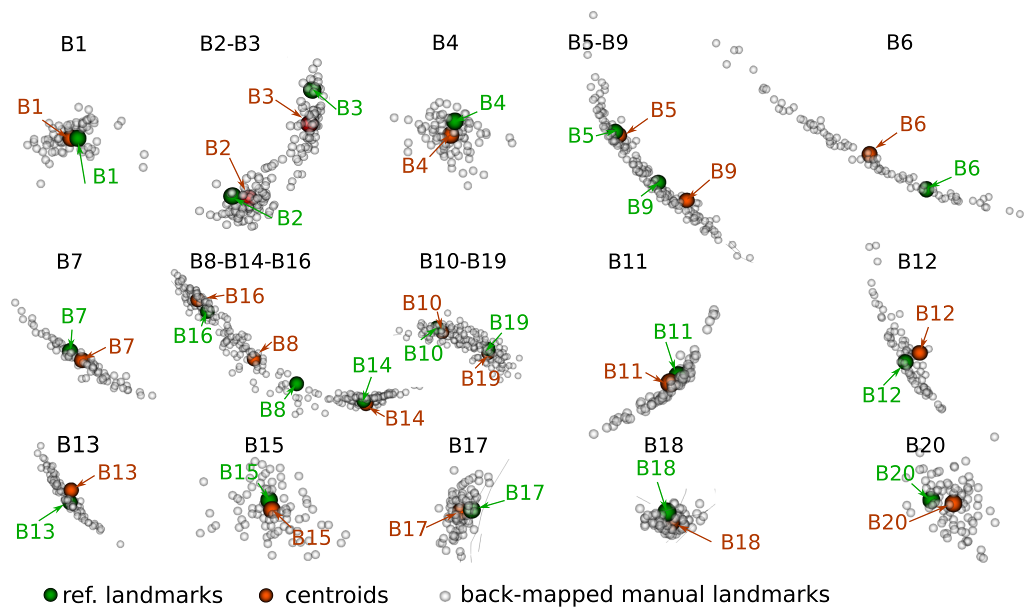

Figure 8: Clouds of manually seeded landmarks mapped onto the template bone.

bioRxiv preprint doi: https://doi.org/10.1101/2020.12.17.423253; this version posted December 18, 2020. The copyright holder for this preprint (which was not certified by peer review) is the author/funder, who has granted bioRxiv a license to display the preprint in perpetuity. It is made available under aCC-BY-NC-ND 4.0 International license.

measured for point B_{12} with a value of 3.62 mm, while the lowest value, 0.677 mm was found for B_{16}. The highest length of confidence for axis y, was found for landmark B_9, with a value of 13.596 mm and the lowest was for landmark B_{18}, with a value of 1.679 mm. The highest length of confidence for axis z, was found for point B_{12}, with a value of 34.978 mm, while the lowest was for landmark B_{18}, with a value of 3.978 mm.

Sex identification Using the DSP2 Method

By using all ten distances M, 87% of males and 98% of females were successfully sexed. The sex was undetermined in 13 male and one female pelvic bone and wrongly assigned to one female. We excluded the distance M_4 from sex identification as it was determined to being the most erroneous, see Figure 7. After excluding M_4, an algorithm assigned 95% of the male pelves and 99% of the female pelves with a 100% accuracy in cases where the sex was assigned, see Table 4.

Table 4: Sex identification results by the DSP2 method (with a 95% posterior probability threshold). The variables on sexing accuracy and sex found to being indeterminable are expressed in %.

		Number of distances M	Sexing Accuracy	Sex Undeterminable	Sexing Error
Male	Original Setting	10	87	13	0
	Corrected data	9	95	5	0
Female	Original Setting	10	98	1	1
	Corrected Data	9	99	1	0

bioRxiv preprint doi: https://doi.org/10.1101/2020.12.17.423253; this version posted December 18, 2020. The copyright holder for this preprint (which was not certified by peer review) is the author/funder, who has granted bioRxiv a license to display the preprint in perpetuity. It is made available under aCC-BY-NC-ND 4.0 International license.

Discussion

Most of the average distances between the manually and automatically seeded landmarks were below 5 mm. Average distances above 5 mm were found for B_6, B_8 and B_9. Landmarks B_6 is defined from the distance M_3 (see the definition in Figure 2), which means it is not directly dependent on bone geometry. Landmark B_6 can be located almost anywhere in the middle third of the iliac crest. The landmark B_8 should lie on a site, where the axis is inserted to the posterior inferior iliac spine just perpendicular to the anterior border of the greater sciatic notch (Figure 2). In this case, the operator's result was superior to that of the computer's result. This can be interpreted as an algorithm employing a similarity metric, which does not take into account any additional geometrical constraints.

The accuracy of automatic landmark seeding depends on the proper seeding of reference landmarks on template bone by an operator. Moreover, the identification of fine anatomical features on template bone can be more difficult because they can be partially smoothed out due to the method used for template bone construction [27]. This situation is typical for landmark B_9, which relies on the location of the anteroinferior termination of the ischial tuberosity.

In our study, the TEM, rTEM and R values were relatively low and the mean differences between the automatic and manually measured distances were within millimetres which is comparable to similar publications [17, 14, 38, 39].

The sex identification results from the DSP2 method, with algorithmic computed input, proved to be very reliable. By leaving out distance M_4 (which is dependent on B_8), we achieved an improved sexing rate of 97% with a 100% accuracy, which is on par with the most relevant studies [14, 39, 38, 40].

The algorithm calculates a continuous spatial transformation, which means that any point on a bone sample has a unique counterpart on the template bone. In other words, we can potentially define landmarks anywhere on the bone [41]. This transformation makes it possible to interpret the difference in shapes in the deformation metric, which is considered as being intuitive and natural. This capability of the registration algorithm allows for shape analysis, which is usually performed by using the Principal Component Analysis (PCA) [42, 43, 44]. Unlike the PCA, the algorithm does not require a correlation matrix, which can be large and dense (in the case of CT data).

bioRxiv preprint doi: https://doi.org/10.1101/2020.12.17.423253; this version posted December 18, 2020. The copyright holder for this preprint (which was not certified by peer review) is the author/funder, who has granted bioRxiv a license to display the preprint in perpetuity. It is made available under aCC-BY-NC-ND 4.0 International license.

In our study, the algorithm took 10 minutes per sample (compiled on a Linux Ubuntu 18.04 LTS platform, GCC 7.4.0, Intel i7 (8 cores) CPU 2.10GHz, 16Gb RAM). This could be seen as a relatively long time, but the pipeline of registration is fully automated and stable, which is very convenient for the end–users. Once the registration step is done, the computing of landmark locations and distances over the whole dataset takes only a few seconds.

We are aware of some study limitations. Contrary to dry bone measurements, thin bone projections and bony plates could potentially be lost in the CT data due to an insufficient resolution and must be carefully reconstructed in order to obtain the same bone topology across the entire dataset. Furthermore, any articular surfaces that may be affected by entesophytes, which is common in the elderly, may reduce the accuracy of automatic landmark placement [45]. A lack of more observers should raise some caution regarding the interpretation of the intraobserver errors, however, a similar setup of the TEM method is proposed in [39, 46, 38].

Conclusion

The anthropological landmarks must be seeded by an experienced operator, even when using CT data. Manually defining anthropological landmarks, especially for larger data sets, is inefficient and can introduce uncertainties depending on the operator's focus on the work at hand as well as his/her level of experience. In this study, we introduced a method that allows us to automate the definition of anthropological landmarks based on a large amount of CT data. This method also makes it possible to potentially use data from bone digitization by laser scanning, which is a subject of further research. In summary, we

- introduced registration algorithm for automatic landmark seeding,
- extensively analysed the differences between manual and automatic landmark seeding, and
- showed the algorithm performance on the task of sex identification.

Conflict of interest statement

The authors declare no conflict of interest.

bioRxiv preprint doi: https://doi.org/10.1101/2020.12.17.423253; this version posted December 18, 2020. The copyright holder for this preprint (which was not certified by peer review) is the author/funder, who has granted bioRxiv a license to display the preprint in perpetuity. It is made available under aCC-BY-NC-ND 4.0 International license.

Acknowledgements

This study was supported by a grant from the Grant Agency of Charles University SVV 260543/2020, Czech Republic. We would like to thank Dr Cyrus Rasti MD for his help in editing the English language content of this article.

References

[1] W. Bass, Missouri archaeological society, Human osteology: a laboratory and field manual. 5th ed. Columbia (MO): Missouri Archaeological Society (2005).

[2] T. D. White, M. T. Black, P. A. Folkens, Human osteology, Academic press, 2011.

[3] K. Krishan, P. M. Chatterjee, T. Kanchan, S. Kaur, N. Baryah, R. Singh, A review of sex estimation techniques during examination of skeletal remains in forensic anthropology casework, Forensic science international 261 (2016) 165–e1.

[4] J. Bruzek, A method for visual determination of sex, using the human hip bone, American Journal of Physical Anthropology: The Official Publication of the American Association of Physical Anthropologists 117 (2002) 157–168.

[5] P. L. Walker, Greater sciatic notch morphology: sex, age, and population differences, American Journal of Physical Anthropology: The Official Publication of the American Association of Physical Anthropologists 127 (2005) 385–391.

[6] M. L. Patriquin, S. Loth, M. Steyn, Sexually dimorphic pelvic morphology in south african whites and blacks, Homo 53 (2003) 255–262.

[7] C. A. King, Osteometric assessment of 20th century skeletons from Thailand and Hong Kong, Universal–Publishers, 1997.

[8] W. S. Enns-Bray, H. Bahaloo, I. Fleps, Y. Pauchard, E. Taghizadeh, S. Sigurdsson, T. Aspelund, P. Büchler, T. B. Harris, V. Gudnason, S. J. Ferguson, H. Pálsson, B. Helgason, Biofidelic finite element models

bioRxiv preprint doi: https://doi.org/10.1101/2020.12.17.423253; this version posted December 18, 2020. The copyright holder for this preprint (which was not certified by peer review) is the author/funder, who has granted bioRxiv a license to display the preprint in perpetuity. It is made available under aCC-BY-NC-ND 4.0 International license.

for accurately classifying hip fracture in a retrospective clinical study of elderly women from the ages reykjavik cohort., Bone 120 (2019) 25–37.

[9] D. Franklin, A. Cardini, A. Flavel, M. K. Marks, Morphometric analysis of pelvic sexual dimorphism in a contemporary western australian population, International journal of legal medicine 128 (2014) 861–872.

[10] M. A. Verhoff, F. Ramsthaler, J. Krähahn, U. Deml, R. J. Gille, S. Grabherr, M. J. Thali, K. Kreutz, Digital forensic osteology—possibilities in cooperation with the virtopsy® project, Forensic science international 174 (2008) 152–156.

[11] M. Sidler, C. Jackowski, R. Dirnhofer, P. Vock, M. Thali, Use of multislice computed tomography in disaster victim identification—advantages and limitations, Forensic science international 169 (2007) 118–128.

[12] S. C. Kuzminsky, M. S. Gardiner, Three-dimensional laser scanning: potential uses for museum conservation and scientific research, Journal of Archaeological Science 39 (2012) 2744–2751.

[13] T. Chapman, P. Lefevre, P. Semal, F. Moiseev, V. Sholukha, S. Louryan, M. Rooze, S. V. S. Jan, Sex determination using the probabilistic sex diagnosis (dsp: Diagnose sexuelle probabiliste) tool in a virtual environment, Forensic science international 234 (2014) 189–e1.

[14] S. Mestekova, J. Bruzek, J. Veleminska, K. Chaumoitre, A test of the dsp sexing method on ct images from a modern french sample, Journal of forensic sciences 60 (2015) 1295–1299.

[15] K. E. Stull, M. L. Tise, Z. Ali, D. R. Fowler, Accuracy and reliability of measurements obtained from computed tomography 3d volume rendered images, Forensic science international 238 (2014) 133–140.

[16] K. L. Colman, A. E. van der Merwe, K. E. Stull, J. G. Dobbe, G. J. Streekstra, R. R. van Rijn, R.-J. Oostra, H. H. de Boer, The accuracy of 3d virtual bone models of the pelvis for morphological sex estimation, International journal of legal medicine 133 (2019) 1853–1860.

[17] K. L. Colman, H. H. de Boer, J. G. Dobbe, N. P. Liberton, K. E. Stull, M. van Eijnatten, G. J. Streekstra, R.-J. Oostra, R. R. van Rijn, A. E. van der Merwe, Virtual forensic anthropology: The accuracy of

bioRxiv preprint doi: https://doi.org/10.1101/2020.12.17.423253; this version posted December 18, 2020. The copyright holder for this preprint (which was not certified by peer review) is the author/funder, who has granted bioRxiv a license to display the preprint in perpetuity. It is made available under aCC-BY-NC-ND 4.0 International license.

osteometric analysis of 3d bone models derived from clinical computed tomography (ct) scans, Forensic science international 304 (2019) 109963.

[18] D. Franklin, A. Cardini, A. Flavel, A. Kuliukas, M. K. Marks, R. Hart, C. Oxnard, P. O'Higgins, Concordance of traditional osteometric and volume-rendered msct interlandmark cranial measurements, International journal of legal medicine 127 (2013) 505–520.

[19] K. Aldridge, S. A. Boyadjiev, G. T. Capone, V. B. DeLeon, J. T. Richtsmeier, Precision and error of three-dimensional phenotypic measures acquired from 3dmd photogrammetric images, American journal of medical genetics Part A 138 (2005) 247–253.

[20] A. R. Klales, S. D. Ousley, J. M. Vollner, A revised method of sexing the human innominate using phenice's nonmetric traits and statistical methods, American journal of physical anthropology 149 (2012) 104–114.

[21] N. J. Tustison, P. A. Cook, A. Klein, G. Song, S. R. Das, J. T. Duda, B. M. Kandel, N. van Strien, J. R. Stone, J. C. Gee, et al., Large-scale evaluation of ants and freesurfer cortical thickness measurements, Neuroimage 99 (2014) 166–179.

[22] B. Dogdas, A. Chen, S. Mehta, T. Shah, B. Robinson, D. Xue, A. Gleason, L. D. Wise, R. Crawford, I. Pak, et al., Characterization of bone abnormalities from micro-ct images for evaluating drug toxicity in developmental and reproductive toxicology (dart) studies, in: 2015 IEEE 12th International Symposium on Biomedical Imaging (ISBI), IEEE, 2015, pp. 671–674.

[23] A. J. Ramme, K. Voss, J. Lesporis, M. S. Lendhey, T. R. Coughlin, E. J. Strauss, O. D. Kennedy, Automated bone segmentation and surface evaluation of a small animal model of post-traumatic osteoarthritis, Annals of biomedical engineering 45 (2017) 1227–1235.

[24] Y. Pauchard, T. Fitze, D. Browarnik, A. Eskandari, I. Pauchard, W. Enns-Bray, H. Pálsson, S. Sigurdsson, S. J. Ferguson, T. B. Harris, et al., Interactive graph-cut segmentation for fast creation of finite element models from clinical ct data for hip fracture prediction, Computer methods in biomechanics and biomedical engineering 19 (2016) 1693–1703.

bioRxiv preprint doi: https://doi.org/10.1101/2020.12.17.423253; this version posted December 18, 2020. The copyright holder for this preprint (which was not certified by peer review) is the author/funder, who has granted bioRxiv a license to display the preprint in perpetuity. It is made available under aCC-BY-NC-ND 4.0 International license.

[25] B. Helgason, S. Gilchrist, O. Ariza, P. Vogt, W. Enns-Bray, R. Widmer, T. Fitze, H. Pálsson, Y. Pauchard, P. Guy, et al., The influence of the modulus–density relationship and the material mapping method on the simulated mechanical response of the proximal femur in side-ways fall loading configuration, Medical engineering & physics 38 (2016) 679–689.

[26] B. B. Avants, P. T. Schoenemann, J. C. Gee, Lagrangian frame diffeomorphic image registration: Morphometric comparison of human and chimpanzee cortex, Medical image analysis 10 (2006) 397–412.

[27] B. B. Avants, N. J. Tustison, G. Song, P. A. Cook, A. Klein, J. C. Gee, A reproducible evaluation of ants similarity metric performance in brain image registration, Neuroimage 54 (2011) 2033–2044.

[28] B. B. Avants, N. Tustison, G. Song, Advanced normalization tools (ants), Insight j 2 (2009) 1–35.

[29] J. Ahrens, B. Geveci, C. Law, Paraview: An end-user tool for large data visualization, The visualization handbook 717 (2005).

[30] J. Bruzek, F. Santos, B. Dutailly, P. Murail, E. Cunha, Validation and reliability of the sex estimation of the human os coxae using freely available dsp2 software for bioarchaeology and forensic anthropology, American journal of physical anthropology 164 (2017) 440–449.

[31] G. Quatrehomme, I. Radoman, L. Nogueira, P. du Jardin, V. Alunni, Sex determination using the dsp (probabilistic sex diagnosis) method on the coxal bone: efficiency of method according to number of available variables, Forensic science international 272 (2017) 190–193.

[32] S. J. Ulijaszek, D. A. Kerr, Anthropometric measurement error and the assessment of nutritional status, British Journal of Nutrition 82 (1999) 165–177.

[33] R. Goto, N. M.-T. CG, Precision of measurement as a component of human variation, Journal of physiological anthropology 26 (2007) 253–256.

[34] S. Carsley, P. C. Parkin, K. Tu, E. Pullenayegum, N. Persaud, J. L. Maguire, C. S. Birken, T. K. Collaboration, et al., Reliability of routinely

bioRxiv preprint doi: https://doi.org/10.1101/2020.12.17.423253; this version posted December 18, 2020. The copyright holder for this preprint (which was not certified by peer review) is the author/funder, who has granted bioRxiv a license to display the preprint in perpetuity. It is made available under aCC-BY-NC-ND 4.0 International license.

collected anthropometric measurements in primary care, BMC medical research methodology 19 (2019) 84.

[35] F. Pedregosa, G. Varoquaux, A. Gramfort, V. Michel, B. Thirion, O. Grisel, M. Blondel, P. Prettenhofer, R. Weiss, V. Dubourg, J. Vanderplas, A. Passos, D. Cournapeau, M. Brucher, M. Perrot, E. Duchesnay, Scikit-learn: Machine learning in Python, Journal of Machine Learning Research 12 (2011) 2825–2830.

[36] P. Murail, J. Bruzek, F. Houët, E. Cunha, Dsp: a tool for probabilistic sex diagnosis using worldwide variability in hip-bone measurements, Bulletins et Mémoires de la Société d'Anthropologie de Paris (2005) 167–176.

[37] S. M. Weinberg, N. M. Scott, K. Neiswanger, M. L. Marazita, Intraobserver error associated with measurements of the hand, American Journal of Human Biology: The Official Journal of the Human Biology Association 17 (2005) 368–371.

[38] E. F. Kranioti, L. Št'ovíčková, M. A. Karell, J. Bruzek, Sex estimation of os coxae using dsp2 software: A validation study of a greek sample, Forensic science international 297 (2019) 371–e1.

[39] E. Vacca, G. Di Vella, Metric characterization of the human coxal bone on a recent italian sample and multivariate discriminant analysis to determine sex, Forensic science international 222 (2012) 401–e1.

[40] A. R. Paz, J. Banner, C. Villa, Validity of the probabilistic sex diagnosis method (dsp) on 3d ct-scans from modern danish population, La Revue de Médecine Légale 10 (2019) 43–49.

[41] M. Málková, J. Parus, I. Kolingerová, B. Beneš, An intuitive polygon morphing, The Visual Computer 26 (2010) 205–215.

[42] L. Savonnet, S. Duprey, S. V. S. Jan, X. Wang, Pelvis and femur shape prediction using principal component analysis for body model on seat comfort assessment. impact on the prediction of the used palpable anatomical landmarks as predictors, PloS one 14 (2019).

bioRxiv preprint doi: https://doi.org/10.1101/2020.12.17.423253; this version posted December 18, 2020. The copyright holder for this preprint (which was not certified by peer review) is the author/funder, who has granted bioRxiv a license to display the preprint in perpetuity. It is made available under aCC-BY-NC-ND 4.0 International license.

[43] S. Kai, T. Sato, Y. Koga, G. Omori, K. Kobayashi, M. Sakamoto, Y. Tanabe, Automatic construction of an anatomical coordinate system for three-dimensional bone models of the lower extremities–pelvis, femur, and tibia, Journal of biomechanics 47 (2014) 1229–1233.

[44] S. Schumann, L.-P. Nolte, G. Zheng, Comparison of partial least squares regression and principal component regression for pelvic shape prediction, Journal of biomechanics 46 (2013) 197–199.

[45] K. L. Colman, J. G. Dobbe, K. E. Stull, J. M. Ruijter, R.-J. Oostra, R. R. Van Rijn, A. E. Van der Merwe, H. H. De Boer, G. J. Streekstra, The geometrical precision of virtual bone models derived from clinical computed tomography data for forensic anthropology, International journal of legal medicine 131 (2017) 1155–1163.

[46] H. M. Karakas, A. Harma, B. Alicioglu, The subpubic angle in sex determination: anthropometric measurements and analyses on anatolian caucasians using multidetector computed tomography datasets, Journal of Forensic and Legal Medicine 20 (2013) 1004–1009.